AIAA JOURNAL
Vol. 43, No. 4, April 2005

Harmonic Balance Approach for an Airfoil with a Freeplay Control Surface

Liping Liu* and Earl H. Dowell†
Duke University, Durham, North Carolina 27708-0300

The nonlinear aeroelastic response of a two-dimensional airfoil, including a control surface with freeplay placed in an incompressible flow, is studied. The model equations are formulated as a set of first-order ordinary differential equations. First, the dynamic response is investigated by a time integration method, and the time integration results are used for the verification of the harmonic balance results. The interesting hysteresis phenomenon and the effect of initial conditions of the subcritical bifurcation are presented. A higher-order harmonic balance method is then derived to investigate the high harmonics of the airfoil motions. The harmonic balance prediction is verified by comparison to the results from a numerical time marching integration and also by comparison to results from a previous experiment.

Nomenclature

a	=	nondimensional distance of the elastic axis from the midchord, with respect to the semichord
$\mathcal{B}$	=	damping submatrix
b	=	semichord
C_h	=	stiffness (per unit span) of wing in deflection
$C(k)$	=	generalized Theodorsen function
C_α, C_β	=	torsional stiffness (per unit span) of wing around a and of aileron around c
c	=	nondimensional distance of the control surface (aileron) hinge line from the midchord, with respect to the semichord
$\mathcal{F}$	=	vector of aerodynamic forces
h	=	plunge displacement
I_α, I_β	=	moments of inertia (per unit span) of wing–aileron and aileron about a and c, respectively
$\mathcal{K}$	=	stiffness submatrix
K_α, K_β	=	torsional structural spring constants (per unit span) for the wing about a and the aileron about c
k	=	reduced frequency, $\omega b/U$
L	=	aerodynamic lift
M	=	mass of wing–aileron (per unit span)
M_α, M_β	=	aerodynamic moments of wing–aileron and aileron about a and c, respectively
m	=	modal mass
r_α, r_β	=	radius of gyration of wing–aileron and reduced radius of gyration of aileron with respect to the semichord
S_α, S_β	=	static moments of wing–aileron and aileron (per unit span) about a and c, respectively
T_i	=	ith Theodorsen constant
U	=	freestream velocity
$\boldsymbol{X}$	=	variable vector
x_α, x_β	=	center of gravity of wing–aileron from a and reduced center of gravity of aileron from c with respect to the semichord
α	=	pitch displacement about the elastic axis
β	=	aileron (flap) displacement about the hinge line (relative to the main wing surface)
δ	=	total angular size of the freeplay region
ζ	=	damping ratio
κ	=	ratio of the mass of a cylinder of air having a diameter equal to the chord of the wing to the mass of the wing, both per unit span
Λ	=	matrix of eigenvectors
λ	=	eigenvalue
ρ	=	density of air
τ	=	nondimensional time $\tau = Ut/b$
ω	=	coupled natural frequency
$\bar{\omega}$	=	uncoupled natural frequency

Subscripts

a	=	aerodynamic component
f	=	value at the flutter point
h	=	value for the entire wing–aileron in the vertical direction
mod	=	modal value
s	=	structural component
α	=	value for the entire wing–aileron about the elastic axis
β	=	value for the aileron about the hinge line

Superscripts

T	=	matrix or vector transpose
-1	=	matrix inverse
$\cdot$	=	first derivative with respect to time t
$\cdot\cdot$	=	second derivative with respect to time t
$'$	=	first derivative with respect to time τ
$''$	=	second derivative with respect to time τ
$\sim$	=	reduced value of aerodynamic forces

I. Introduction

LIMIT cycle oscillations (LCOs) and bifurcations arising from a concentrated structural nonlinearity in the restoring forces were first studied by Woolston et al.,[1] Shen,[2] and Küssner.[3] A comprehensive review of the bifurcations and chaos of the three basic nonlinearities, namely, cubic, freeplay, and hysteresis has been reported in Ref. 4. The first-order harmonic balance (HB) method (including only one dominant harmonic in the analysis), often referred to as the describing function (DF) approach or the equivalent linearization technique, cannot predict higher harmonic response.[5,6] A major finding of the study in Ref. 7 is that a surprisingly large number of harmonics is needed to describe the secondary bifurcation

Received 18 May 2004; revision received 4 November 2004; accepted for publication 4 November 2004.

*Postdoctoral Fellow, Department of Mechanical Engineering and Materials Science.

†J. A. Jones Professor, Department of Mechanical Engineering and Materials Science. Fellow AIAA.

for an airfoil with a cubic spring in the pitch degree of freedom. The present study focuses on a two-dimensional airfoil including a control surface with a freeplay nonlinearity placed in an incompressible flow. An experimental model that closely approximates the three degrees of freedom typical section in two-dimensional incompressible flow has been built, and flutter tests of the two-dimensional wing model with control surface freeplay were performed in the Duke University low-speed wind tunnel. An excellent description of the experimental model is provided by Conner et al.[8] Results obtained from the direct time integration of the nonlinear differential equations were shown in Refs. 5, 8, and 9 to be in good agreement with the experimental measurements.

Note that two different theoretical models have been used for the same experimental model. A reduced-order finite state aerodynamic model based on Peters's finite state model for the two-dimensional aerodynamic flow over an airfoil has been applied to the nonlinear aerodynamic system (see Refs. 5 and 9). By the use of a small number of these aerodynamic modes, the aeroelastic model was formed by coupling them to a typical section structural model with a trailing-edge flap and including a freeplay nonlinearity in the flap rotation. In Ref. 8, however, the equations of motion for the three degrees of freedom typical section are cast in the state-space form. That formulation includes the two augmented states required for Jones's approximation of Wagner's indicial loading function that yields an approximation to the generalized Theodorsen function. In the present study, a slightly different and simpler model is used for the two-dimensional incompressible flow with the details presented in the following section. The theoretical model is then formulated as a set of first-order ordinary differential equations. Continuing and extending the DF approach carried out by Tang et al.,[5] a general formulation of the HB method is derived in the present paper to account for the freeplay nonlinearity in the structure. The higher harmonics of the airfoil motions are investigated by the HB method. The analytical prediction is verified by comparisons to the results from a numerical time marching integration and the previous experimental results.[5,8,9] Furthermore, the higher-order HB prediction improves on previous DF results.[5]

II. Equations of Airfoil Motions

The model here is a three-degree-of-freedom airfoil section with nonlinear structural freeplay in flap rotation. A schematic of the typical airfoil section with a control surface at the trailing edge of the main wing is shown in Fig. 1a, and a freeplay structural nonlinearity of the control surface is shown in Fig. 1b. There are three degrees of freedom: plunge h, pitch α, and flap β. Figure 1a shows one of the classical problems in nonlinear aeroelasticity. By the use of standard procedures, the equations in pitch, flap, and plunge, respectively, can be written as[10]

$$I_\alpha\ddot{\alpha} + [I_\beta + b(c-a)S_\beta]\ddot{\beta} + S_\alpha\ddot{h} + C_\alpha\alpha = M_\alpha$$

$$[I_\beta + b(c-a)S_\beta]\ddot{\alpha} + I_\beta\ddot{\beta} + S_\beta\ddot{h} + C_\beta M(\beta) = M_\beta$$

$$S_\alpha\ddot{\alpha} + S_\beta\ddot{\beta} + M_{\text{total}}\ddot{h} + C_h h = L \tag{1}$$

where the dot denotes the real time derivatives. The left-hand side of the equations represents the structural components, and the right-hand side represents the aerodynamic forcing. The parameter definitions are given in the Nomenclature. With a structural freeplay gap, the control surface-restoring moment-rotation relationships may be expressed as

$$M(\beta) = \begin{cases} \beta + \delta, & \beta < -\delta \\ 0, & -\delta < \beta < \delta \\ \beta - \delta, & \beta > \delta \end{cases} \tag{2}$$

The key values used for the nondimensionalization are the mass per unit span of the entire airfoil M and the semichord b. The

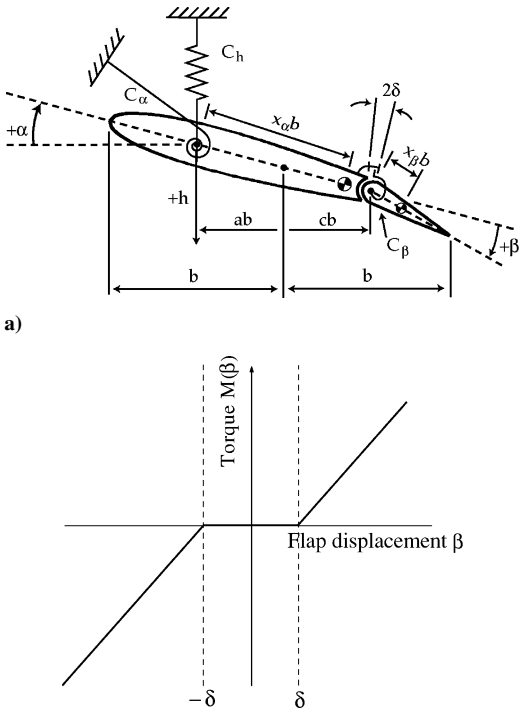

Fig. 1 Typical airfoil section with a) control surface and b) freeplay nonlinearity.

nondimensional form of the structural equations is[8]

$$r_\alpha^2\ddot{\alpha} + \left[r_\beta^2 + (c-a)x_\beta\right]\ddot{\beta} + x_\alpha\ddot{h} + r_\alpha^2\omega_\alpha^2\alpha = \tilde{M}_\alpha$$

$$\left[r_\beta^2 + (c-a)x_\beta\right]\ddot{\alpha} + r_\beta^2\ddot{\beta} + x_\beta\ddot{h} + r_\beta^2\omega_\beta^2 M(\beta) = \tilde{M}_\beta$$

$$x_\alpha\ddot{\alpha} + x_\beta\ddot{\beta} + (M_{\text{total}}/M)\ddot{h} + \omega_h^2 h = \tilde{L} \tag{3}$$

where $\tilde{M}_\alpha = M_\alpha/Mb^2$, $\tilde{M}_\beta = M_\beta/Mb^2$, and $\tilde{L} = L/Mb$. The expressions of the nondimensionalized system parameters in Eq. (3) are given in Appendix A.

In a vector form, the linearization of system (3) is

$$\mathcal{M}_s\ddot{\boldsymbol{X}} + \mathcal{K}_s\boldsymbol{X} = \boldsymbol{\mathcal{F}}$$

where

$$\mathcal{M}_s = \begin{pmatrix} r_\alpha^2 & r_\beta^2 + (c-a)x_\beta & x_\alpha \\ r_\beta^2 + (c-a)x_\beta & r_\beta^2 & x_\beta \\ x_\alpha & x_\beta & \dfrac{M_{\text{total}}}{M} \end{pmatrix}$$

$$\mathcal{K}_s = \begin{pmatrix} r_\alpha^2\omega_\alpha^2 & 0 & 0 \\ 0 & r_\beta^2\omega_\beta^2 & 0 \\ 0 & 0 & \omega_h^2 \end{pmatrix}, \qquad \boldsymbol{\mathcal{F}} = \begin{pmatrix} \tilde{M}_\alpha \\ \tilde{M}_\beta \\ \tilde{L} \end{pmatrix}$$

A minimal amount of structural damping has been included in the equations model. The procedure is outlined as follows, and the reader is referred to Ref. 8 for more details. A structural damping is included in the system by adding a damping submatrix similar in form to $\mathcal{M}_s$ and $\mathcal{K}_s$:

$$\mathcal{M}_s\ddot{\boldsymbol{X}} + \mathcal{B}_s\dot{\boldsymbol{X}} + \mathcal{K}_s\boldsymbol{X} = \boldsymbol{\mathcal{F}}$$

where $\mathcal{B}_s$ is computed by $\mathcal{B}_s = (\Lambda^T)^{-1}\mathcal{B}_{\text{mod}}(\Lambda)^{-1}$ and

$$\mathcal{B}_{\text{mod}} = \begin{pmatrix} 2m_1\omega_1\zeta_1 & 0 & 0 \\ 0 & 2m_2\omega_2\zeta_2 & 0 \\ 0 & 0 & 2m_3\omega_3\zeta_3 \end{pmatrix}$$

where ζ_i are the measured damping ratios. The model mass m_i and the coupled natural frequency ω_i are computed as follows, where $i = 1, 2, 3$:

1) Find eigenvalues λ_i and eigenvectors Λ from the system $\mathcal{M}_s\ddot{\boldsymbol{X}} + \mathcal{K}_s\boldsymbol{X} = 0$.

2) Then, $\omega_i = \sqrt{\lambda_i}$.

3) $\mathcal{M}_{\text{mod}} = \Lambda^T \mathcal{M}_s \Lambda$, and m_i are the values at the diagonal entries of $\mathcal{M}_{\text{mod}}$.

For an incompressible flow, the aerodynamic forces are adopted from Ref. 10 as follows:

$$
\begin{aligned}
M_\alpha &= -\rho b^2\Big\{\pi\Big(\tfrac{1}{2}-a\Big)Ub\dot{\alpha} + \pi b^2\Big(\tfrac{1}{8}+a^2\Big)\ddot{\alpha} \\
&\quad + (T_4+T_{10})U^2\beta + \Big[T_1 - T_8 - (c-a)T_4 + \tfrac{1}{2}T_{11}\Big]Ub\dot{\beta} \\
&\quad - [T_7 + (c-a)T_1]b^2\ddot{\beta} - a\pi b\ddot{h}\Big\} + 2\rho U b^2\pi\Big(a+\tfrac{1}{2}\Big)C(k) \\
&\quad \times \Big\{U\alpha + \dot{h} + b\Big(\tfrac{1}{2}-a\Big)\dot{\alpha} + (1/\pi)T_{10}U\beta + b(1/\pi)T_{11}\dot{\beta}\Big\} \\
M_\beta &= -\rho b^2\Big\{\Big[-2T_9 - T_1 + T_4\Big(a-\tfrac{1}{2}\Big)\Big]Ub\dot{\alpha} + 2T_{13}b^2\ddot{\alpha} \\
&\quad + (1/\pi)U^2\beta(T_5 - T_4T_{10}) - (1/2\pi)Ub\dot{\beta}T_4T_{11} \\
&\quad - (1/\pi)T_3b^2\ddot{\beta} - T_1b\ddot{h}\Big\} - \rho U b^2 T_{12}C(k)\Big[U\alpha + \dot{h} \\
&\quad + b\Big(\tfrac{1}{2}-a\Big)\dot{\alpha} + (1/\pi)T_{10}U\beta + b(1/2\pi)T_{11}\dot{\beta}\Big] \\
L &= -\rho b^2(U\pi\dot{\alpha} + \pi\ddot{h} - \pi ba\ddot{\alpha} - UT_4\dot{\beta} - T_1b\dot{\beta}) \\
&\quad - 2\pi\rho UbC(k)\Big\{U\alpha + \dot{h} + b\Big(\tfrac{1}{2}-a\Big)\dot{\alpha} \\
&\quad + (1/\pi)T_{10}U\beta + b(1/2\pi)T_{11}\dot{\beta}\Big\} \qquad (4)
\end{aligned}
$$

They are functions of the structural states of the system (α, β, h), their time derivatives, the generalized Theodorsen function, and a set of Theodorsen constants that arise from the integration of velocity potentials that are used to define the aerodynamics around the airfoil. The definitions of the Theodorsen constants T_i, $i = 1, 2, \ldots, 11$, are given in Appendix B. Details of the generalized Theodorsen function $C(k)$ can be found in Ref. 10. Here, k is the reduced frequency of oscillation, $k = \omega b/U$. An approximation to the Wagner function is used to simplify the mathematical expression for Theodorsen aerodynamics while maintaining the most important physical characteristics. Here the Wagner function $\phi(\tau)$ is given by Jones's approximation (see Ref. 11)

$$\phi(\tau) = 1 - \psi_1 e^{-\varepsilon_1\tau} - \psi_2 e^{-\varepsilon_2\tau}$$

with the constants $\psi_1 = 0.165$, $\psi_2 = 0.335$, $\varepsilon_1 = 0.0455$, and $\varepsilon_2 = 0.3$. A nondimensional time $\tau = Ut/b$ and six new variables are introduced to eliminate the integral terms in the aeroelastic system:

$$
\begin{aligned}
w_1(\tau) &= \int_0^\tau e^{-\varepsilon_1(\tau-\sigma)}\alpha(\sigma)\,\mathrm{d}\sigma, \qquad w_2(\tau) = \int_0^\tau e^{-\varepsilon_2(\tau-\sigma)}\alpha(\sigma)\,\mathrm{d}\sigma \\
w_3(\tau) &= \int_0^\tau e^{-\varepsilon_1(\tau-\sigma)}\beta(\sigma)\,\mathrm{d}\sigma, \qquad w_4(\tau) = \int_0^\tau e^{-\varepsilon_2(\tau-\sigma)}\beta(\sigma)\,\mathrm{d}\sigma \\
w_5(\tau) &= \int_0^\tau e^{-\varepsilon_1(\tau-\sigma)}\xi(\sigma)\,\mathrm{d}\sigma, \qquad w_6(\tau) = \int_0^\tau e^{-\varepsilon_2(\tau-\sigma)}\xi(\sigma)\,\mathrm{d}\sigma
\end{aligned} \qquad (5)
$$

where ε_1 and ε_2 are the constants in the Wagner function, and $\xi = h/b$ is the nondimensional plunge deflection. The original aeroelastic system (1), written in a complete nondimensional form, is

$$
\begin{aligned}
&A_1\alpha'' + A_2\beta'' + A_3\xi'' + A_4\alpha' + A_5\beta' + A_6\xi' + A_7\alpha + A_8\beta \\
&\quad + A_9\xi + A_{11}w_1 + A_{12}w_2 + A_{13}w_3 + A_{14}w_4 \\
&\quad + A_{15}w_5 + A_{16}w_6 = f(\tau) \\
&B_1\alpha'' + B_2\beta'' + B_3\xi'' + B_4\alpha' + B_5\beta' + B_6\xi' + B_7\alpha + B_8\beta \\
&\quad + B_9\xi + B_{10}M(\beta) + B_{11}w_1 + B_{12}w_2 + B_{13}w_3 + B_{14}w_4 \\
&\quad + B_{15}w_5 + B_{16}w_6 = g(\tau) \\
&C_1\alpha'' + C_2\beta'' + C_3\xi'' + C_4\alpha' + C_5\beta' + C_6\xi' + C_7\alpha + C_8\beta \\
&\quad + C_9\xi + C_{11}w_1 + C_{12}w_2 + C_{13}w_3 + C_{14}w_4 \\
&\quad + C_{15}w_5 + C_{16}w_6 = h(\tau) \qquad (6)
\end{aligned}
$$

Here the prime denotes the derivative with respect to the nondimensional time τ. The coefficients A_i, B_i, and C_i, $i = 1, 2, 3, \ldots, 16$, are functions of the airfoil parameters, and their expressions are given in Appendix C. The expressions for the right-hand sides of Eqs. (6) are

$$
\begin{aligned}
f(\tau) &= -2\kappa\Big(a+\tfrac{1}{2}\Big)\Big[\xi(0) + \Big(\tfrac{1}{2}-a\Big)\alpha(0) + (T_{11}/2\pi)\beta(0)\Big] \\
&\quad \times \Big(\psi_1\varepsilon_1 e^{-\varepsilon_1\tau} + \psi_2\varepsilon_2 e^{-\varepsilon_2\tau}\Big) \\
g(\tau) &= (1/\pi)T_{12}\kappa\Big[\xi(0) + \Big(\tfrac{1}{2}-a\Big)\alpha(0) + (T_{11}/2\pi)\beta(0)\Big] \\
&\quad \times \Big(\psi_1\varepsilon_1 e^{-\varepsilon_1\tau} + \psi_2\varepsilon_2 e^{-\varepsilon_2\tau}\Big) \\
h(\tau) &= 2\kappa\Big[\xi(0) + \Big(\tfrac{1}{2}-a\Big)\alpha(0) + (T_{11}/2\pi)\beta(0)\Big] \\
&\quad \times \Big(\psi_1\varepsilon_1 e^{-\varepsilon_1\tau} + \psi_2\varepsilon_2 e^{-\varepsilon_2\tau}\Big) \qquad (7)
\end{aligned}
$$

By the introduction of a variable vector $\boldsymbol{X} = (x_1, x_2, \ldots, x_{12})^T$ with $x_1 = \alpha$, $x_2 = \alpha'$, $x_3 = \beta$, $x_4 = \beta'$, $x_5 = \xi$, $x_6 = \xi'$, $x_7 = w_1$, $x_8 = w_2$, $x_9 = w_3$, $x_{10} = w_4$, $x_{11} = w_5$, and $x_{12} = w_6$, the coupled equations given in Eq. (6) can be written as a set of 12 first-order ordinary differential equations written in vector form:

$$\boldsymbol{X}' = F(\boldsymbol{X}, \tau) \qquad (8)$$

This approach allows existing methods suitable for the study of ordinary differential equations to be used in the analysis. For large values of τ, transients are damped out and steady-state solutions are obtained: $f(\tau) = 0$, $g(\tau) = 0$, and $h(\tau) = 0$. Therefore, for the steady-state solutions, the investigation in Secs. III and IV.B focuses on system (6) with zero right-hand sides. However, the explicit equation (7) is considered in the numerical investigation in Sec. IV.A.

III. Higher-Order HB Method

The main idea of the HB method is to balance the Fourier components of several dominant harmonics based on the assumption of a periodic limit cycle. Note that higher-order harmonic terms can be retained in the HB model, allowing for periodic responses other than simple harmonic motion. Once the motions are assumed to be harmonic, the Fourier components of the motions derivatives and the integrals of the motions can be obtained in a straightforward manner. A possible difficulty with the application of the HB technique to a freeplay nonlinearity may exist in finding the Fourier components of the nonlinear force $M(\beta)$. This difficulty has been overcome in this study by introducing two more augmented variables. The time histories of the flap rotation motion and its corresponding force for one period are displayed in Fig. 2a. Here, the period is normalized to be 2π: $\hat{t} = \omega\tau$, thus, the normalized time $\hat{t}$ varies from 0 to 2π. Assume that the steady-state flap motion starts from the highest amplitude ($\hat{t} = 0$). The flap rotation angle then decreases until $\beta = \delta$ ($\hat{t} = t_1$) and keeps decreasing, crossing zero until $\beta = -\delta$ ($\hat{t} = t_2$). In the negative direction, the flap moves to its negative maximum angle ($\hat{t} = \pi$), after which it changes its rotating direction and moves toward its mean position. Then the flap angle increases, crossing $\beta = -\delta$ and $\beta = \delta$ until the positive maximum angle ($\hat{t} = 2\pi$), from which the cycle repeats. Assume that the motion is symmetric about its mean position; therefore, the corresponding times for the last two crossing points are $\hat{t} = 2\pi - t_2$ and $\hat{t} = 2\pi - t_1$, respectively. Corresponding

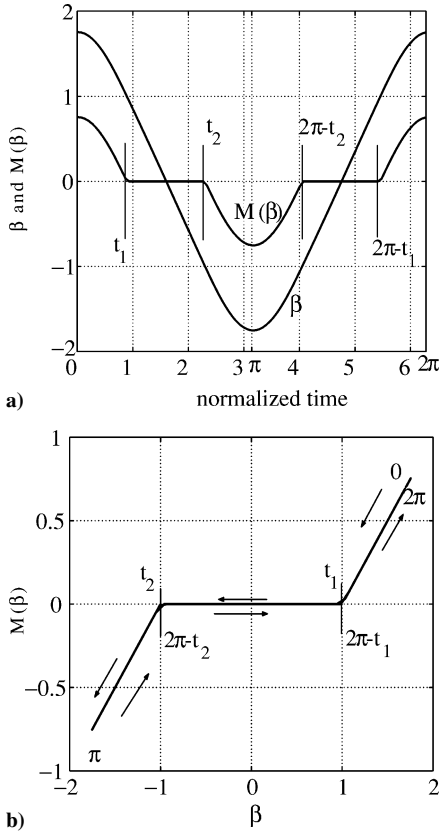

Fig. 2 One period (normalized to be 2π) of flap rotation and corresponding moment displayed in a) time history and b) moment vs displacement.

to the flap rotation in one period, the response force experiences one period as well. The moment $M(\beta)$ starts from its positive maximum ($\hat{t}=0$), decreases to zero ($\hat{t}=t_1$), remains zero in the freeplay region (until $\hat{t}=t_2$), decreases to its negative maximum, then increases to zero ($\hat{t}=2\pi-t_2$), remains zero in the freeplay region (until $\hat{t}=2\pi-t_1$), and finally increases to its positive maximum ($\hat{t}=2\pi$). The whole cycle then repeats. The flap motion and the moments during one cycle are displayed in Fig. 2b. From Fig. 2b, we have

$$M(\beta)=\begin{cases}\beta-\delta, & \hat{t}\in[0,\ t_1]\cup[2\pi-t_1,\ 2\pi]\\ 0, & \hat{t}\in[t_1,\ t_2]\cup[2\pi-t_2,\ 2\pi-t_1]\\ \beta+\delta, & \hat{t}\in[t_2,\ 2\pi-t_2]\end{cases} \tag{9}$$

where t_1 and t_2 are two augmented variables. In most cases, t_1 varies from 0 to $\pi/2$ and t_2 varies from $\pi/2$ to π. With Eq. (9), the Fourier components of the flap moment are easy to obtain:

$$M(\beta)=M_0+\sum_{n=1}^{N}\left(M_{s_n}\sin n\omega\tau+M_{c_n}\cos n\omega\tau\right)$$

$$M_0=\frac{1}{2\pi}\left\{\int_0^{t_1}[\beta(\hat{t})-\delta]\,\mathrm{d}\hat{t}+\int_{2\pi-t_1}^{2\pi}[\beta(\hat{t})-\delta]\,\mathrm{d}\hat{t}+\int_{t_2}^{2\pi-t_2}[\beta(\hat{t})+\delta]\,\mathrm{d}\hat{t}\right\}$$

$$M_{s_n}=\frac{1}{\pi}\left\{\int_0^{t_1}[\beta(\hat{t})-\delta]\sin(n\hat{t})\,\mathrm{d}\hat{t}+\int_{2\pi-t_1}^{2\pi}[\beta(\hat{t})-\delta]\sin(n\hat{t})\,\mathrm{d}\hat{t}+\int_{t_2}^{2\pi-t_2}[\beta(\hat{t})+\delta]\sin(n\hat{t})\,\mathrm{d}\hat{t}\right\}$$

$$M_{c_n}=\frac{1}{\pi}\left\{\int_0^{t_1}[\beta(\hat{t})-\delta]\cos(n\hat{t})\,\mathrm{d}\hat{t}+\int_{2\pi-t_1}^{2\pi}[\beta(\hat{t})-\delta]\cos(n\hat{t})\,\mathrm{d}\hat{t}+\int_{t_2}^{2\pi-t_2}[\beta(\hat{t})+\delta]\cos(n\hat{t})\,\mathrm{d}\hat{t}\right\} \tag{10}$$

Now assume that the motions are of the form

$$\alpha=a_0+\sum_{n=1}^{N}(a_n\sin n\omega\tau+b_n\cos n\omega\tau)$$

$$\beta=c_0+c_1\cos\omega\tau+\sum_{n=2}^{N}(c_n\sin n\omega\tau+d_n\cos n\omega\tau)$$

$$\xi=e_0+\sum_{n=1}^{N}(e_n\sin n\omega\tau+f_n\cos n\omega\tau) \tag{11}$$

The Fourier components of the time derivatives and the integral terms for the pitch motion are

$$\alpha'=n\omega\sum_{n=1}^{n=N}(a_n\cos n\omega\tau-b_n\sin n\omega\tau)$$

$$\alpha''=-n^2\omega^2\sum_{n=1}^{N}(a_n\cos n\omega\tau+b_n\sin n\omega\tau)$$

$$w_1=\frac{a_0}{\varepsilon_1}+\sum_{n=1}^{N}\frac{\varepsilon_1}{\varepsilon_1^2+(n\omega)^2}(a_n\sin n\omega\tau+b_n\cos n\omega\tau)+\sum_{n=1}^{N}\frac{n\omega}{\varepsilon_1^2+(n\omega)^2}(b_n\sin n\omega\tau-a_n\cos n\omega\tau)$$

$$w_2=\frac{a_0}{\varepsilon_2}+\sum_{n=1}^{N}\frac{\varepsilon_2}{\varepsilon_2^2+(n\omega)^2}(a_n\sin n\omega\tau+b_n\cos n\omega\tau)+\sum_{n=1}^{N}\frac{n\omega}{\varepsilon_2^2+(n\omega)^2}(b_n\sin n\omega\tau-a_n\cos n\omega\tau) \tag{12}$$

For the other two degrees of freedom, flap and plunge, similar expressions can be obtained, and they are given in Appendix D.

By substitution of

$$\beta(\hat{t})=c_0+c_1\cos(\hat{t})+\sum_{n=2}^{N}[c_n\sin(n\hat{t})+d_n\cos(n\hat{t})]$$

into Eq. (10), the expressions of the Fourier components for the flap moment can be obtained. General expressions for M_0, M_{s_n}, and M_{c_n} cannot be obtained. However, for the cases studied in this paper, the exact expressions are given in Appendix E. The two augmented variables satisfy the following conditions:

$$\frac{\delta-c_0}{c_1}=\cos(t_1)+\sum_{n=2}^{N}\left[\frac{c_n}{c_1}\sin(nt_1)+\frac{d_n}{c_1}\cos(nt_1)\right]$$

$$\frac{-\delta-c_0}{c_1}=\cos(t_2)+\sum_{n=2}^{N}\left[\frac{c_n}{c_1}\sin(nt_2)+\frac{d_n}{c_1}\cos(nt_2)\right] \tag{13}$$

We then substitute the expressions from Eqs. (11) and (12), Appendix D, Eq. (10), and Appendix E into system (6), with zero right-hand sides. Collecting the coefficients of $\sin n\omega\tau$ and $\cos n\omega\tau$, $n=0,1,\ldots,N$, yields an algebraic system of $6N+3$ equations with variables ω; a_n, c_n, and e_n, $n=0,1,\ldots,N$; b_n and

f_n, $n = 1, 2, \ldots, N$; d_n, $n = 2, 3, \ldots, N$; and t_i, $i = 1, 2$. There are $6N + 5$ variables. Therefore, Eqs. (13) have to be included in the system of the Fourier coefficients.

Because the freeplay nonlinearity is piecewise linear, the system of $6N + 5$ equations is strictly linear in all of the Fourier coefficients. Therefore, the system can always be reduced to three nonlinear equations in the fundamental frequency ω and the two augmented variables t_i, $i = 1, 2$. A more detailed explanation is given in the following section.

IV. Results and Discussion

The results obtained from a direct time marching integration of the nonlinear ordinary differential equations (8) are presented and compared with previous numerical time integration and experimental results. The first- and third-order HB approaches derived in Sec. III are applied to system (6), and the results are compared with numerical time integration, previous DF, and experimental results. The theoretical calculations are performed for the set of system parameters corresponding to the experimental model to observe the efficiency and limitation of the theoretical models and methods. A complete list of the system parameters for the experimental model[8] is given in Table 1.

A. Time Marching Integration Results

A key issue in the time marching integration of a piecewise linear system is accurately integrating to the "switching points" where the change in linear subdomains occurs. A standard time marching scheme, for example, the Runge–Kutta method, with uniform time step may lead to inconsistent or even incorrect numerical results. There are several approaches to account for the abrupt stiffness change: Hénon's method,[12] the Runge–Kutta algorithm in conjunction with Hénon's method (see Refs. 13 and 14), and the adaptive time steps with linear interpolation or bisection.[15,16]

In this study, a recently developed approach, the point transformation (PT) method[17] is adapted to the study of the three-degrees-of-freedom system. System (8) consists of three subsystems that are strictly linear in their subdomains. The exact solutions in each subdomain can be expressed analytically. Briefly, the PT formulation can be described as follows: Starting with a given set of initial conditions, the traveling time in the current subdomain is computed by solving a single nonlinear algebraic equation; the switching points for the motion crossing to its next subdomain are calculated by the multiplication of a known matrix by a known vector. Detailed procedures of the PT technique can be found in Ref. 17. The PT method has the advantage of classic time marching integrations for the consideration of initial effects and transient states. Obtaining the traveling time from a single nonlinear equation, the PT method only needs four time steps for one loop of the motion. By the use of large time steps and integration to the exact switching points, the PT method removes the limitation of classic time marching schemes.

Table 1 System parameters used in simulation

Parameter	Value
Geometry	
Chord	0.254 m
Span	0.52 m
Semichord b	0.127
Elastic axis a with respect to b	−0.5
Hinge line c with respect to b	0.5
Mass (inertial)	
Mass of wing	0.62868 kg
Mass of aileron	0.18597 kg
Mass/length of wing–aileron	1.558 kg
Mass of support blocks	0.47485 × 2 kg
S_α (per span)	0.08587 kg m
S_β (per span)	0.00395 kg m
x_α	0.434
x_β	0.01996
I_α (per span)	0.01347 kg m^2
I_β (per span)	0.0003264 kg m^2
Stiffness	
K_α (per span)	37.3 kg m/s^2
K_β (per span)	3.9 kg m/s^2
K_h (per span)	2818.8 kg/m/s^2
Damping	
ζ_1 (half-power)	0.01626
ζ_2 (half-power)	0.0115
ζ_3 (half-power)	0.0113
Frequency	
ω_1 (coupled)	9.21 Hz
ω_2 (coupled)	19.44 Hz
ω_3 (coupled)	4.45 Hz

1. Results for the Linear System ($\delta = 0$ deg)

When the freeplay region is sufficiently small such that the effect can be neglected, that is, $\delta = 0$, the aeroelastic system (8) becomes strictly linear. The stability of the system response is thus determined by the eigenvalues of the coefficient matrix. For a small flow velocity, the real parts of the eigenvalues of the matrix are negative, indicating convergent system motions. When the flow velocity crosses certain value, some eigenvalues may have positive real parts, indicating divergent system motions. The critical value of the flow velocity, when the eigenvalues cross through the imaginary axis from the negative half-plane to the positive half-plane, is the flutter velocity indicating the instability of the wing model.

With various flap stiffness K_β, a flutter boundary is obtained in Fig. 3a that shows the flutter velocities of the linear system vs the flap stiffness from 0 to 2.05 kg · m^2/s^2. Note that the flutter boundary changes little for $K_\beta > 2.05$. Compared to Fig. 2(a) in Ref. 5, the results from two different theoretical models for the aerodynamics are essentially the same. The flutter value that corresponds to zero stiffness ($K_\beta = 0$ and $\omega_\beta = 0$) in this study is 7.6 m/s, slightly smaller than 8.6 m/s in Ref. 5. The minimum flutter velocity for any stiffness occurs at $K_\beta = 0.1$ kg · m^2/s^2 or $\omega_\beta/\omega_\alpha = 0.46$ (Fig. 4), exactly the same as that in Ref. 5. The minimum flutter velocity value (3.5 m/s), however, is smaller than that (4.5 m/s) in Ref. 5. For large stiffness

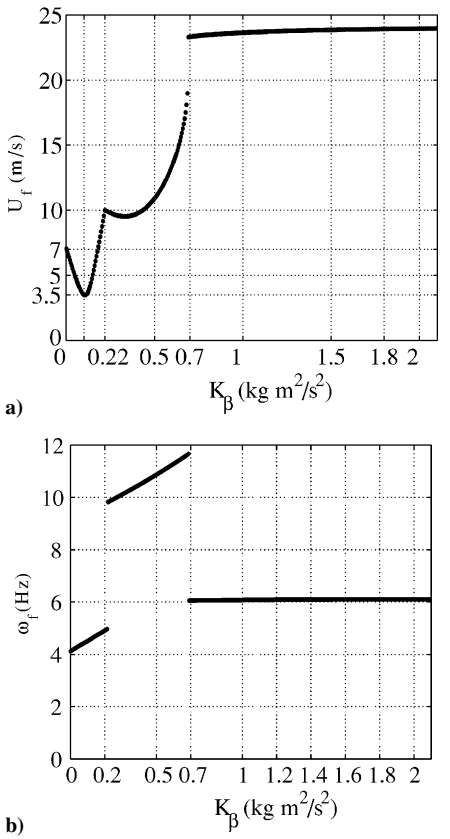

Fig. 3 Time marching results: a) flutter velocity vs nominal flap stiffness and b) flutter frequency.

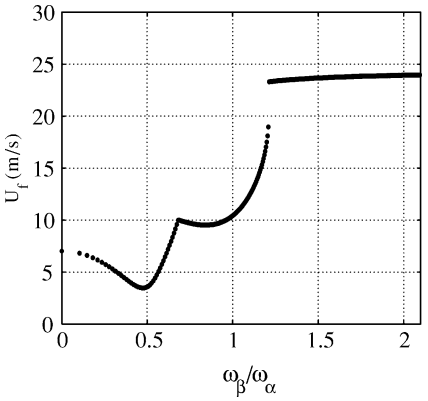

Fig. 4 Time marching results: flutter velocity vs natural frequency ratio.

($K_\beta > 2$), the flutter velocity approaches $U_f = 23.9$ m/s, identical to the result in Ref. 5.

The flutter velocity vs the uncoupled frequency ratio $\omega_\beta/\omega_\alpha$ is shown in Fig. 4. As mentioned in Ref. 5 for $\omega_\beta/\omega_\alpha < 1.2$, there are two distinct flutter boundaries corresponding to the pitch dominated and plunge dominated motions. For large $\omega_\beta/\omega_\alpha > 1.2$, there is only one flutter velocity that corresponds to the plunge dominated motion. Figure 4 shows the most critical flutter velocity, the lowest flutter value.

Correspondingly, the flutter frequency is shown in Fig. 3b. There are two abrupt changes in the flutter frequency near $K_\beta = 0.29$ and 0.7, corresponding to the two abrupt changes in the flutter boundary shown in Figs. 3a and 4. Figure 3b is exactly the same as Fig. 2c in Ref. 5. Both aerodynamic models predict the frequency very well. This also indicates that the frequency is not as sensitive as other variables, for example, flutter velocities, to the details of the aerodynamic model. From Figs. 3 and 4, as the stiffness K_β increases, the flutter first occurs in the plunge dominated motion ($K_\beta \in [0,\ 0.29]$), then in the pitch dominated motion ($K_\beta \in [0.29,\ 0.7]$), and, finally, back to the plunge dominated motion ($K_\beta > 0.7$).

2. Results for the Nonlinear System ($\delta = 1.0$ deg)

For the nonlinear system, a specific freeeplay configuration is chosen that corresponds to a nominal angular gap of 2.0 deg, that is, $\delta = 1.0$ deg. However, as noted in Refs. 5, 8, and 9, all responses scale in proportion to δ. Therefore, the results for the amplitudes are normalized by the angular gap in the following discussions. To compare with the results in the preceding study, the flow velocities in Figs. 5–10, 11a, and 12 are normalized by $U_f \equiv 8.6$ m/s. In this study, attention is focused on one typical case with a flap stiffness higher than the pitch stiffness, that is, $\omega_\beta/\omega_\alpha = 2.1$.

a. Amplitudes and frequencies of LCOs. The classical flutter velocity for this configuration with no freeplay is 23.9 m/s. System motions are divergent for the velocities beyond the flutter speed. When a freeplay is present, however, there are various types of nonzero motions for the velocity below the flutter speed, including LCOs with or without higher harmonics and chaos. The time marching integration results shown in Figs. 5–10 and 13–15 are for the initial condition $\beta(0) = 2.0$ deg and other zero initial values. The increment in the velocity ratio is 0.01.

After the transients die down, the local extremes (α when $\alpha' = 0$, β when $\beta' = 0$, and ξ when $\xi' = 0$) of the time series of each degree of freedom are recorded, and the results are shown in Figs. 5b and 6 for various flow velocities. If two local extremes are found for one velocity, for example, $U/U_f = 2.0$, the system motion is close to a sine wave. If, for a given velocity, for example, $U/U_f = 0.6$, in the pitch motion, the number of points found is more than two but still a finite number. The higher harmonic components in the motion may not be neglected. If one or more vertical line segments are found for one velocity, for example, $U/U_f = 1.2$, then the peak values of the motion cycles are not fixed. The motion loop never repeats itself, and, therefore, the motion is nonperiodic. As discussed in Ref. 8,

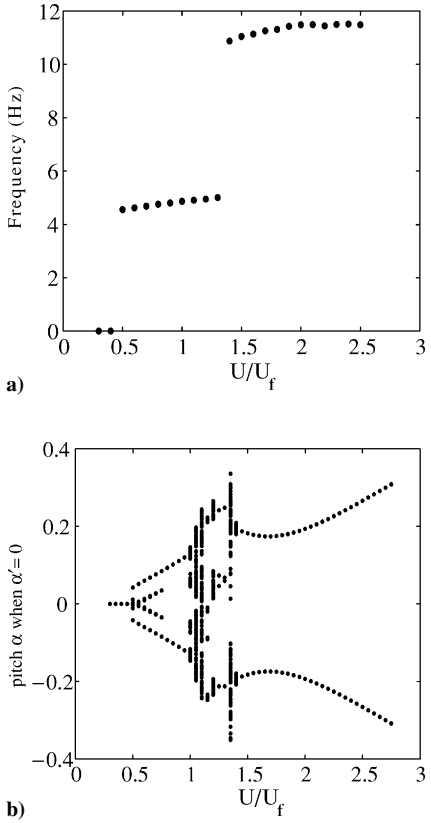

Fig. 5 Time marching results, bifurcation diagram for a) frequency and b) pitch angle.

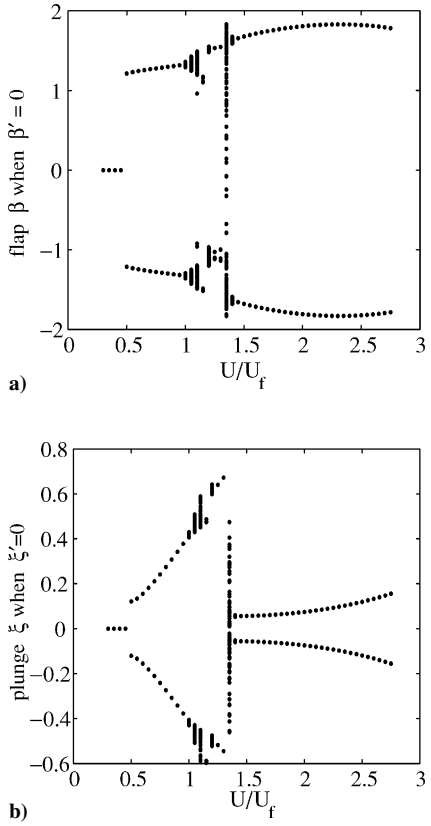

Fig. 6 Time marching results, bifurcation diagram for a) flap rotation and b) plunge deflection.

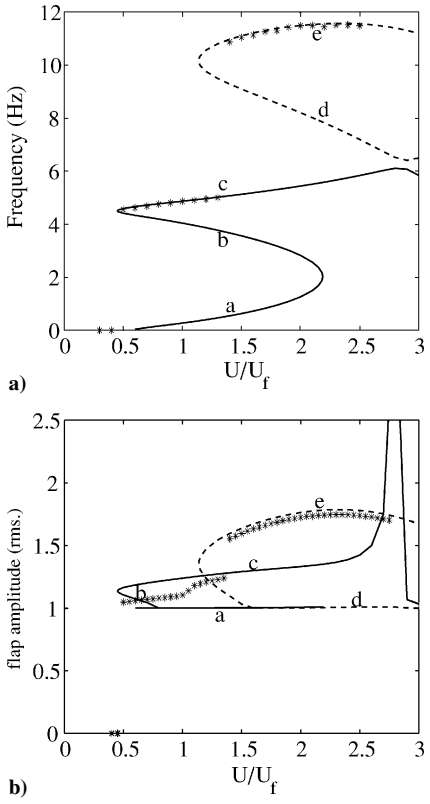

Fig. 7 Comparison of results from numerical time integration and HB1: a) frequency and b) flap amplitude: ∗, time marching results; ——, HB1 results for low-frequency motions; and - - - -, HB1 results for high-frequency motions.

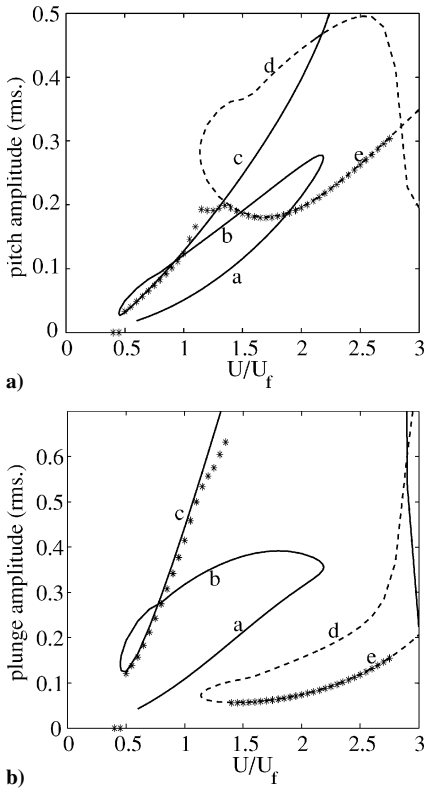

Fig. 8 Comparison of results from numerical time integration and HB1: a) pitch amplitude and b) plunge amplitude: ∗, time marching results; ——, HB1 results for low-frequency motions; and - - - -, HB1 results for high-frequency motions.

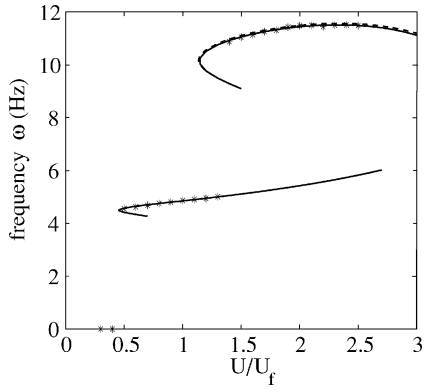

Fig. 9 Comparison of results from time marching integration and harmonic balance predictions for frequency: ∗, time marching results; - - - -, HB1 results; and ——, HB3 results.

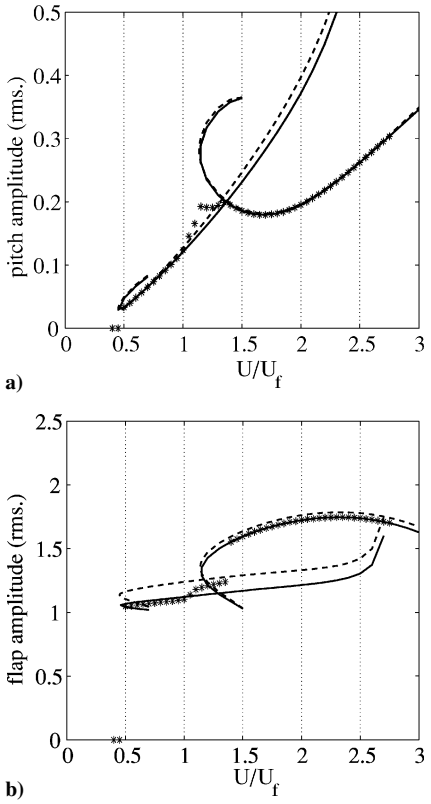

Fig. 10 Comparisons of results from time marching integration and harmonic balance prediction for a) pitch angle motion and b) flap rotation motion: ∗, time marching results; - - - -, HB1 results; and ——, HB3 results.

for a small flow velocity, the nonzero initial excitation decays, and the motion settles down at the zero mean position. When started at $U/U_f = 0.5$, the zero motion becomes unstable, and the nonzero disturbance results in an LCO with small amplitude. The motions remain periodic until $U = U_f$, after which the motions are nonperiodic. For the range of flow velocity $1.0U_f < U < 1.4U_f$, vertical line segments are present for each velocity. From the phase path and power spectral density (PSD) plot of the motion in Fig. 13, the motions are thought to be quasi periodic. When the velocity increases beyond $1.4U_f$ yet remains below the flutter speed for $K_\beta \to \infty$, that is, 23.9 m/s, the motion settles down to a simple periodic LCO with two local extremes per cycle. From the bifurcation diagrams in Figs. 5b and 6, the mean positions of the motions may not always be zero. The numerical computation reveals that the mean value for the flap rotation for $U/U_f = 1.15$ is nonzero. Therefore, it is necessary to include a_0, c_0, and e_0 in the motion assumption (11).

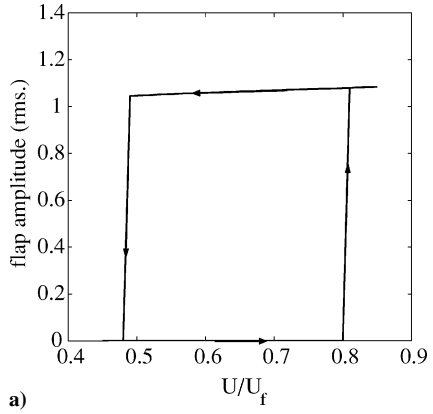

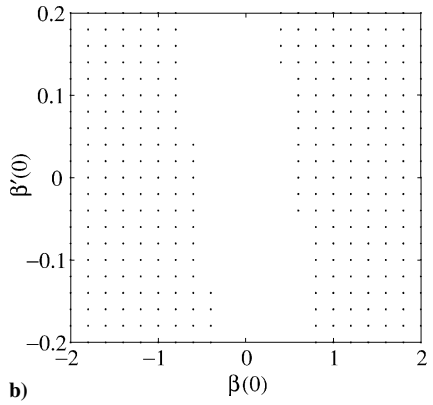

Fig. 11 Time marching results: a) hyeteresis phenomenon and b) basin of attraction (dot: LOC) for $U/U_f = 0.7$, $\alpha(0) = \alpha'(0) = \xi(0) = \xi'(0) = 0$, $\beta(0) \in [-2 \text{ deg}, 2 \text{ deg}]$, and $\beta'(0) \in [-0.2, 0.2]$.

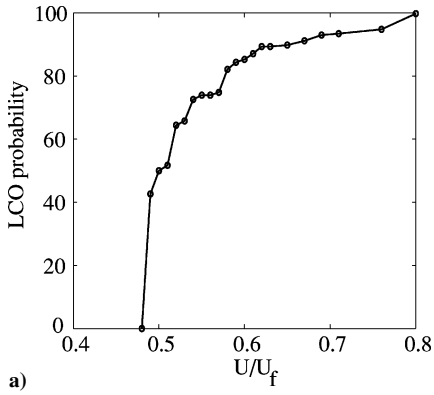

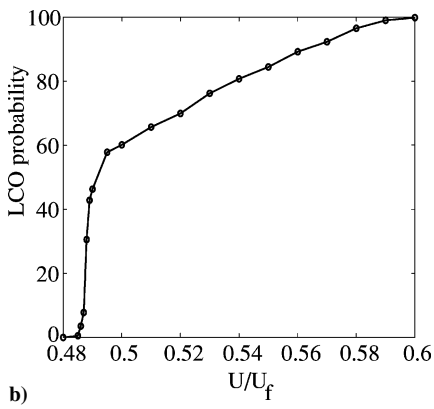

Fig. 12 Time marching results, jump probability for various flow velocities for a) various initial pitch, $\alpha(0) \in [-10 \text{ deg}, 10 \text{ deg}]$ and $\alpha'(0) \in [-1, 1]$ and b) various initial plunge, $\xi(0) \in [-0.5, 0.5]$ and $\xi'(0) \in [-0.05, 0.05]$.

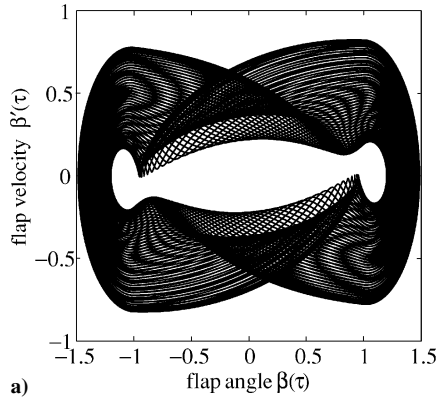

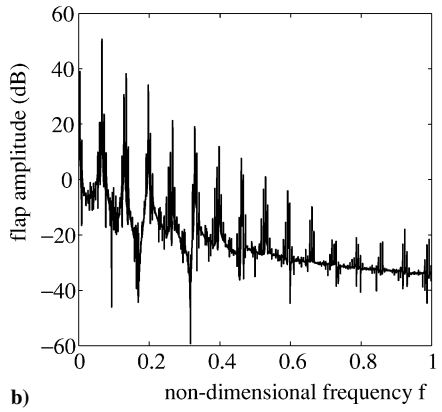

Fig. 13 Time marching results, time series for $U = 1.1U_f$: a) phase path of flap rotation angle and b) PSD plot of motion in part a.

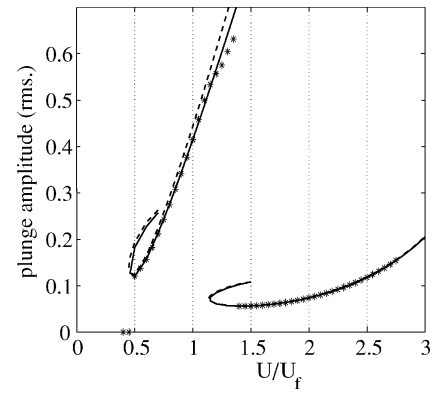

Fig. 14 Comparisons of results from time marching integration and harmonic balance prediction for plunge motion: ∗, time marching results; - - - -, HB1 results; and ——, HB3 results.

The fundamental frequency in Fig. 5a is obtained by taking the highest peak of the PSD plot of the motion series. For the motion with zero amplitudes, that is, zero motion, the frequency is assumed to be zero. There are two abrupt changes/jumps: one at $U/U_f = 0.5$ when the zero motion becomes unstable and the system motion settles down at an LCO and the other one at $U/U_f = 1.4$, when the system motion changes from nonperiodic to periodic motion. The frequency value of the first branch is near the plunge natural frequency, whereas the value of the second branch is near the pitch natural frequency. The motions in the regime $U/U_f \in [1.0, 1.4]$ are considered to be mildly chaotic, which is the reason that the fundamental frequency can be obtained from the PSD plot. Note that the fundamental frequency for the nonperiodic motions remains on the first branch of the frequency curve, and no abrupt change is found in the frequency when the system response changes from periodic to nonperiodic motion. This result is different from the results in Ref. 8, where the changes in the frequency are found when the motion types change.

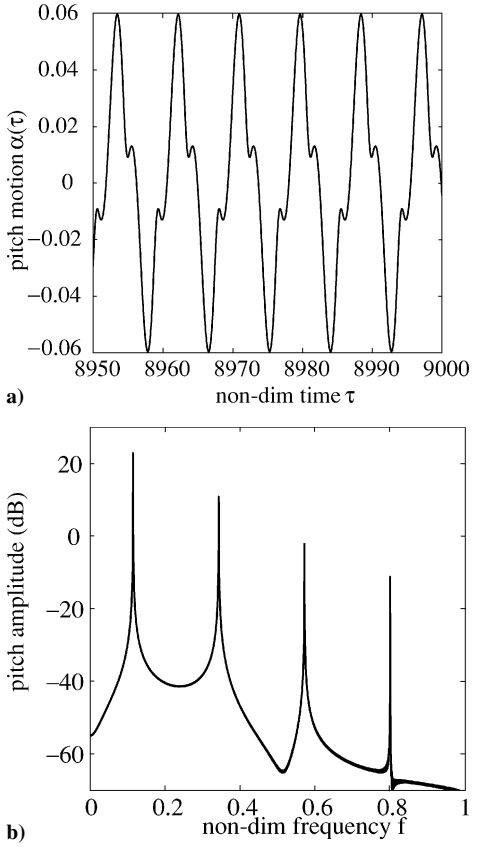

Fig. 15 Time marching results, typical pitch motion for $U = 0.6U_f$ and $\beta(0) = 2$ deg, $\alpha(0) = \alpha'(0) = \beta'(0) = \xi(0) = \xi'(0) = 0$: a) time history and b) power spectral density.

To compare with the earlier theoretical and experimental results, the rms amplitude of the motions is also obtained in Figs. 7, 8, 10, and 14. The formula of the rms amplitude used in this study is

$$y_{\text{mean}} = \frac{1}{n}\sum_{i=1}^{i=n} y_i, \qquad y_{\text{rms}} = \sqrt{\frac{1}{n}\sum_{i=1}^{i=n}(y_i - y_{\text{mean}})^2}$$

where n is the number of points taken to calculate the amplitude. Here n is large, such that $n\Delta t$ covers several complete motion cycles, and y is α, β, or ξ. For nonperiodic motion, convergence in the mean and rms was obtained to within the size of the plotted data points. The rms results in this study appear to be almost identical to the results in Ref. 8. Note that the normalizing bases in amplitudes and flow velocities therein are different. There is a slight difference between the rms result here and the result in Ref. 8. Similar to the frequency curve, there are three branches in the amplitude curve and only two abrupt jumps are observed at $U = 0.5U_f$ and $1.4U_f$. The rms results of the complicated motions in the regime $U/U_f \in [1.0, 1.4]$ remain on the second branch and seem to be continuous with the rms of the periodic motions for $U/U_f \in [0.5, 1.0]$.

b. Hysteresis phenomenon. The primary bifurcation at $U = 0.5U_f$ is a subcritical bifurcation, for which a hysteresis phenomenon is likely to occur. In this study, a hysteresis phenomenon is discovered in the first jump of the motion at $U = 0.5U_f$, whereas no hysteresis is observed in the second jump at $U = 1.4U_f$. Starting with a small flow velocity, for example, $U = 0.2U_f$, and with a very small initial disturbance, the flow velocity may be increased until the motion jumps to a nonzero LCO at $U = 0.8U_f$. This is the lower branch of the hysteresis. To trace the upper branch of the hysteresis, one may start with a large flow velocity, for example, $U = 0.9U_f$, and with a nonzero disturbance. The motion settles down at the LCO on the second branch of the bifurcation. When the LCO is slightly disturbed with a slightly smaller velocity, the motion settles down at another LCO on the same branch. The disturbed LCO remains on the nonzero branch until $U = 0.47U_f$, when the motion dies down to zero. The hysteresis of the flap rotation is shown in Fig. 11 in terms of the rms amplitude vs the velocity. Because the system is coupled, the hysteresis branches for the other degrees of freedom are from $U = 0.47U_f$ to $U = 0.8U_f$ as well.

c. Effect of initial conditions. The preceding discussion of the hysteresis phenomenon suggests that for flow velocities between $U = 0.47U_f$ and $0.8U_f$, a certain disturbance is required to excite the LCO, whereas for $U > 0.8U_f$, any infinitesimal disturbance will lead to an LCO on the upper branch of the bifurcation. The values of the initial conditions required to excite the LCO can only be determined by time integration. No experimental data have been obtained to verify the theoretical results. By extension of the study in Ref. 5, where only the initial displacement of each degree of freedom was considered, a more detailed investigation is carried out in this study to account for both the initial displacement and velocity for each degree of freedom. To define fully the initial conditions, at least the six structural states should be given. However, it is fair to assume that the nonzero initial conditions are stated for only a few states, whereas all others are zero.

The effect of the initial condition in the flap rotation is displayed in Fig. 11b. The initial flap angle and the initial flap angle velocity vary in a certain range: $\beta(0) \in [-2 \text{ deg}, 2 \text{ deg}]$ and $\beta'(0) \in [-0.2, 0.2]$, and the flow velocity is $U = 0.7U_f$. A dot represents the onset of the LCO, otherwise it represents zero motion. In Fig. 11b, most of the points are with dots, indicating that the system motions with most initial disturbances in the flap angle settle down at LCOs. For large initial flap angle $|\beta(0)| > 0.8$ deg, the steady states are LCOs for all flap angle velocity $\beta'(0)$, including zero velocity $\beta'(0) = 0$. For $0.4 < |\beta(0)| < 0.8$ deg, however, the smaller the initial flap angle is, the larger is the initial flap angle velocity needed to excite LCOs. For very small initial flap angles $|\beta(0)| < 0.4$ deg, no LCO is found in the range of the initial flap angle velocity considered in this study.

For the pitch degree of freedom, the hysteresis branch lasts from $U = 0.47U_f$ to $0.8U_f$. The basin of attraction is shown in Fig. 16 for two typical flow velocities, $U = 0.5U_f$ and $0.7U_f$. Unlike the flap rotation angle where the onset of the LCO mainly depends on the initial angle displacement, the effect of the initial pitch angle in Fig. 16 appears rather complex. Briefly, for a small initial pitch angle displacement, a large initial pitch angle velocity may excite an LCO. However, in Fig. 16a, for the flow velocity $U = 0.5U_f$, there are small islands of zero motions. The existence of the zero motion islands far away from the origin indicates that, for large initial pitch angle displacement and angle velocity, the motion may not be excited to an LCO. However, for the same flow condition, a small initial pitch angle displacement $\alpha(0)$ and velocity $\alpha'(0)$ may be able to excite an LCO. This is a surprising and interesting result. As the flow velocity increases the far away islands of zero motions disappear (Fig. 16b). However, the effect of initial pitch angle velocity cannot be neglected because there are islands of zero motions for small initial pitch angle $\alpha(0) \in [-2 \text{ deg}, 2 \text{ deg}]$.

To have an overall idea of the chances of the motion settling down at LCOs when the initial values vary in certain range, a probability curve is constructed based on the time integration results and is shown in Fig. 12a for the effect of initial conditions in the pitch degree of freedom. The curve can be made smoother if finer grids in the mesh of initial conditions are used in the calculation. The probability is obtained by the following formula:

$$p = \frac{\text{number of dots}}{\text{number of overall mesh points}} \times 100 \tag{14}$$

From Fig. 12, the chance of settling down at LCOs increases rapidly from 0 to 50% in the range from $U = 0.48U_f$ to $0.5U_f$. After $U = 0.5U_f$, the probability increases gradually until almost 100% at $U = 0.8U_f$, after which the LCO is excited under any finite disturbance. The relationship between the probability and the flow velocity appears to be roughly parabolic in Fig. 12a.

The hysteresis branch for the plunge degree of freedom is rather short, from $U = 0.47U_f$ to $0.6U_f$. The basin attractions are

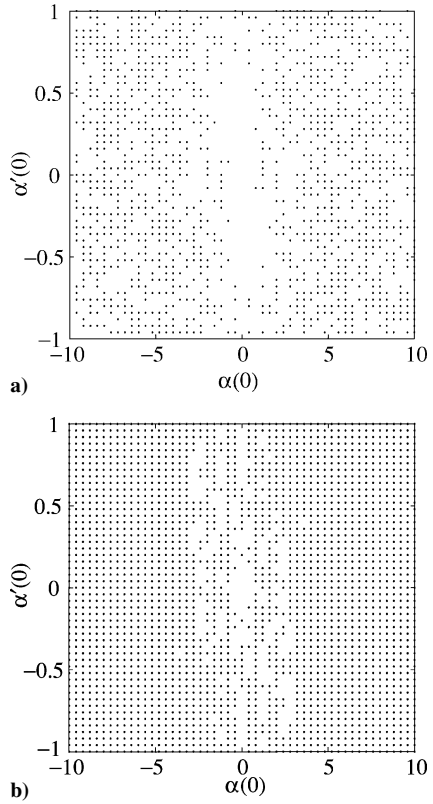

Fig. 16 Time marching results, basins of attractions for a) $U/U_f = 0.5$ and b) $U/U_f = 0.7$; $\beta(0) = \beta'(0) = \xi(0) = \xi'(0) = 0$, $\alpha(0) \in [-10$ deg, 10 deg], and $\alpha'(0) \in [-1.0, 1.0]$ (dot: LCO).

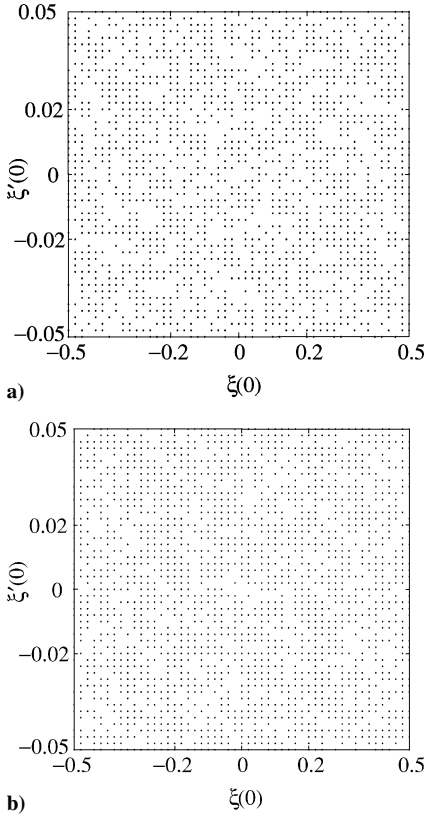

Fig. 17 Time marching results, basins of attractions for a) $U/U_f = 0.5$ and b) $U/U_f = 0.52$: $\alpha(0) = \alpha'(0) = \beta(0) = \beta'(0) = 0$, $\xi(0) \in [-0.5, 0.5]$, and $\xi'(0) \in [-0.05, 0.05]$ (dot: LCO).

displayed in Fig. 17, and the probability curve is shown in Fig. 12b. The effect of the initial plunge displacement and velocity is more complex compared to that in the other two degrees of freedom. Small islands of zero motions appear irregularly in the considered range of initial plunge: $\xi(0) \in [-0.5, 0.5]$ and $\xi'(0) \in [-0.05, 0.05]$. Moreover, with $\xi(0) = 0.06$ and $\xi'(0) = 0$ taken for an example, for the flow condition $U = 0.5U_f$ in Fig. 17a, an LCO is obtained, whereas when the flow velocity increases to $U = 0.52U_f$ in Fig. 17b, a zero motion is obtained. Nonetheless, the chances for the LCOs increase as the flow velocity increases. Similar to the pitch angle, the probability increases rapidly from 0 to 60% as U increases from $0.47U_f$ to $0.5U_f$, after which the probability increases gradually as U increases from $0.5U_f$ to $0.6U_f$. The relationship between the probability and velocity appears to be linear for the plunge initial conditions.

B. HB Results

Because of the assumption of periodic motion, the analytical HB technique is not capable of detecting chaos. With this restriction in mind, the results obtained from the use of the HB1 (HB including one harmonic) and HB3 (HB including three harmonics) are reported for the nonlinear system and compared with the time integration results discussed in the preceding subsection. Before the HB method is applied to the system for the LCO predictions, some time integration motions are analyzed, and the results are shown in Fig. 15 for $U = 0.6U_f$. From Fig. 15, the higher harmonic components are not negligible, and the frequency of the second dominant harmonic is three times that of the first (fundamental) harmonic. The PSD plots of the motions on the bifurcation branches for $U \in [0.5U_f, U_f]$ and for $U \in [1.4U_f, 2.5U_f]$ are similar to Fig. 15b, and they all show that the second dominant harmonic is 3ω, where ω is the fundamental harmonic. Therefore, in the following discussion, the mean positions a_0, c_0, and e_0 are kept in the motion assumption (11), and the HB3 includes only the harmonics of ω and 3ω. To compare with the previous results in Refs. 5 and 8, the motion amplitudes are scaled to rms amplitudes in the following discussion.

1. *HB1 Results*

Assume that the motion forms are

$$\alpha(\tau) = a_0 + a_1 \sin\omega\tau + b_1 \cos\omega\tau, \qquad \beta(\tau) = c_0 + c_1 \cos\omega\tau$$
$$\xi(\tau) = e_0 + e_1 \sin\omega\tau + f_1 \cos\omega\tau \tag{15}$$

The Fourier components of the derivatives of each degree of freedom, the integral terms, and the freeplay flap moment are then obtained from Eq. (12) with $N = 1$ and from Eq. (E1) in Appendix E. By substitution of these expressions into system (6) with zero right-hand sides and the collection of the coefficients of 1, $\sin\omega\tau$ and $\cos\omega\tau$ yield a system of 9 equations with 11 unknowns, including the Fourier coefficients, the fundamental frequency ω, and the two augmented variables $t_i, i = 1, 2$. The condition on the two augmented variables is

$$\delta = c_0 + c_1 \cos t_1, \qquad -\delta = c_0 + c_1 \cos t_2 \tag{16}$$

The algebraic expressions in the equations of the Fourier components are cumbersome. However, the main relationships among the variables are rather simple as shown in Table 2. In Table 2, HB1 equations (1–3) are from the first equation in system (6) for the coefficients of 1, $\sin\omega\tau$, and $\cos\omega\tau$, respectively. Similarly, HB1 equations (4–6) are from the second equation in system (6), and HB1 equations (7–9) are from the third equation in system (6). Note that because $M_{s_1} = 0$ in Eq. (E1), the augmented variables t_1 and t_2 do not appear in HB1 equation (5), the coefficients of $\sin\omega\tau$ in the second equation of system (6). The procedure for reducing the high-dimensional system to solve for the frequency and amplitudes for the LCOs is as follows:

1) Consider the system of HB1 equations (2), (3), (5), (8), and (9) that are linear in variables a_1, b_1, c_1, e_1, and f_1. Set the determinant of this system to be zero. A single nonlinear algebraic equation for ω is then obtained. Solve the frequency equation for ω.

Table 2 Variables and relationships in equations of HB1 system in Sec. IV.B.1

Equation	Variable	Relationship
(1)	a_0, e_0, c_0	Linear
(2)	a_1, b_1, c_1, e_1, f_1	Linear
(2)	ω	Nonlinear
(3)	a_1, b_1, c_1, e_1, f_1	Linear
(3)	ω	Nonlinear
(4)	a_0, e_0, c_0	Linear
(4)	t_1, t_2	Nonlinear
(5)	a_1, b_1, c_1, e_1, f_1	Linear
(5)	ω	Nonlinear
(6)	a_1, b_1, c_1, e_1, f_1	Linear
(6)	t_1, t_2, ω	Nonlinear
(7)	a_0, e_0, c_0	Linear
(8)	a_1, b_1, c_1, e_1, f_1	Linear
(8)	ω	Nonlinear
(9)	a_1, b_1, c_1, e_1, f_1	Linear
(9)	ω	Nonlinear

2) Solve the linear system of HB1 equations (2), (3), (8), and (9) for a_1, b_1, e_1, and f_1 in terms of c_1. Solve the linear system of HB1 equations (1) and (7) for a_0 and e_0 in terms of c_0.

3) Replace HB1 equation (4) by $M_0 = 0$, an equation in t_1 and t_2. After the results from steps 1 and 2 are substituted into system (6), the equation can be written as $v(t_1, t_2)c_1 = 0$.

4) Solve the system of equations $M_0 = 0$ and $v(t_1, t_2) = 0$ for t_1 and t_2.

5) Solve system (16) for c_0 and c_1.

6) Substitute the result from step 5 into the result in step 2 to compute the solutions for the other Fourier coefficients. The HB1 result is then obtained.

In step 1, a single nonlinear algebraic equation for the fundamental frequency ω is obtained. After some complex algebraic manipulation that can be done by a standard symbolic software, for example, Maple,[18] the frequency equation turns out to be a 14th-degree polynomial in x, where $x = \omega^2$. Maple can find 14 roots. The use of the positive roots while the negative, zero, and complex roots of x are neglected yields physically meaningful solutions of $\omega = \sqrt{x}$. Each solution of ω yields one solution for each Fourier coefficient because the system is linear in these latter variables.

The results are shown in Figs. 7 and 8 for the frequency and the rms amplitudes. There are two curves: one denoted by solid lines for the low-frequency motions and the other denoted by dashed lines for the high-frequency motions. The lines and the turning points are correlated. For example, the solutions for ω on branch a in Fig. 7a lead to the solutions for the amplitudes on branch a in Fig. 7b for the flap, on branch a in Fig. 8a for the pitch, and on branch a in Fig. 8b for the plunge.

From Figs. 7 and 8, the branches c and e are in a good agreement with the time integration results. However, there are solutions that are physically impossible, for example, branches a and d in Fig. 8b, when it is noted that the flap freeplay region is from -1 to 1 deg. The physically meaningless solutions can be avoided by imposing a restriction on the solutions of the two augmented variables, that is, $t_1 \in [0, \pi/2]$ and $t_2 \in [\pi/2, \pi]$. The results after imposing this condition are shown in Figs. 9, 10, and 14, in which the HB1 results are denoted by dashed lines, so as to be distinguished from the HB3 results. From Figs. 9, 10, and 14, parts of branches b and d in Figs. 7 and 8 remain in the HB1 results. A closer inspection determines that the condition imposed on t_1 and t_2 excludes only the 1-deg results on the flap and the corresponding results in ω, the pitch, and the plunge.

The HB1 results denoted by dashed lines in Figs. 9, 10, and 14 agree well with the DF and, thus, the experimental results in Ref. 8, except for the lower line in Fig. 9 for $U \in [1.4U_f, 2.7U_f]$ and the corresponding results in amplitudes, which did not appear in earlier DF, time integration, or experimental results. The part of the HB results where the corresponding time integration results cannot be found is believed to represent unstable LCOs. A detailed proof of this is omitted here.

A good prediction for the frequency is obtained. In Fig. 9, the HB1 result is in excellent agreement with the time integration result. From Figs. 10a and 14, the HB1 results for the pitch and plunge for $U \in [0.5U_f, U_f]$ and $U \in [1.4U_f, 2.7U_f]$ match the time integration results well. The corresponding HB1 result in the flap, however, shows some deviation: The HB1 predictions are slightly higher than the time integration result. Note that the deviation of the HB1 results for the amplitudes of the motions in $U \in [U_f, 1.4U_f]$ remains small. Because the motions are found to be nonperiodic and with higher harmonics, a significant discrepancy is expected between the HB1 and the time integration results for $U \in [U_f, 1.4U_f]$.

2. *HB3 Results*

Because there are deviations between the HB1 and the time integration results, and because the PSD plot for some of the time series shows evidence of higher harmonics, more harmonics need to be included in the HB analysis. In this subsection, the second dominant harmonic 3ω is included, and the result improves on the HB1 result in Sec. IV.B.1.

Similar to the derivation in Sec. IV.B.1 with $N = 3$, Eq. (E2) in Appendix E, and the coefficients of the second harmonic 2ω set to zero, the relationship of the Fourier components is obtained as a system of 15 equations. Furthermore, system (16) becomes

$$\begin{aligned} \delta &= c_0 + c_1 \cos t_1 + c_3 \sin 3t_1 + d_3 \cos 3t_1 \\ -\delta &= c_0 + c_1 \cos t_2 + c_3 \sin 3t_1 + d_3 \cos 3t_2 \end{aligned} \tag{17}$$

A table similar to Table 2 can be obtained with six more equations for the coefficients of high harmonic 3ω. Note that for HB3, the sine component of the first harmonic in the force $M(\beta)$ is nonzero, that is, $M_{s_1} \neq 0$ in Eq. (E2), and a single equation of the fundamental frequency ω can no longer be derived. The procedure for HB3 is slightly different from that in Sec. IV.B.1:

1) Solve the linear system of two equations in (a_0, c_0, e_0) for (a_0, e_0) in terms of c_0. Solve the linear system of four equations in $(a_1, b_1, c_1, e_1, f_1)$ for (a_1, b_1, e_1, f_1) in terms of c_1. Solve the linear system of four equations in $(a_3, b_3, c_3, d_3, e_3, f_3)$ for (a_3, b_3, e_3, f_3) in terms of (c_3, d_3).

2) After substitution of the results from step 1 into the other five equations, these five equations are linear in (c_1, c_3, d_3), and nonlinear in (ω, t_1, t_2).

3) The system of five equation obtained from step 2 is homogeneous. Assuming $c_1 \neq 0$, we define $s_1 = c_3/c_1$ and $s_2 = d_3/c_1$. The system (inhomogeneous) is then linear in (s_1, s_2). Arbitrarily choose two equations to solve for (s_1, s_2), and substitute the resulting expressions into the remaining three equations. A system of three equations nonlinear in (ω, t_1, t_2) is then obtained. Solve the reduced three-dimensional system for (ω, t_1, t_2).

4) Substitute the solutions of (ω, t_1, t_2) into the expressions of (s_1, s_2) obtained from step 3 to obtaine the solutions of (s_1, s_2).

5) Substitute the solutions of (t_1, t_2, s_1, s_2) into system (17) to solve for (c_0, c_1). Then $c_3 = s_1 c_1$ and $d_3 = s_2 c_1$.

6) Substitute the result from step 5 into the result from step 2 to compute the solutions for the other Fourier coefficients. The HB3 result is then obtained.

To reduce the computational cost in solving the reduced three-dimensional system in step 3 for (ω, t_1, t_2), the HB1 results for ω, t_1, and t_2 are used as the initial guess in the iteration to solve the nonlinear system. The other steps of the procedure can be carried out in a straightforward manner.

The HB3 results are shown in Figs. 9, 10, and 14 and are denoted by solid lines. The lower branch of the frequency remains unchanged. The HB3 result for the upper branch improves on the corresponding HB1 result: In Fig. 9, the solid line is slightly lower than the dashed line and matches the time integration results better than the dashed line does. Similarly, for the amplitudes, the HB3 results remain the same as the HB1 results when the HB1 results already match the time integration results well; and the HB3 results improve the agreement between the HB and time integration results when the HB1 results vary from the numerical results. In particular,

in Fig. 10b for the flap, the solid line of the second branch is lower than the dashed line and matches the time integration results well. The solid line of the first branch is also lower than the dashed line, and the deviation between the HB3 and the time integration results becomes small.

In summary, for $U \in [0.5U_f, U_f]$ of the first branch, although including more high harmonics for example, HB5, may improve the prediction, the deviation of the HB3 results from the time integration results is small, and the turning point of the HB results is slightly different from that in Fig. 11a. Note that, for $U \in [U_f, 1.4U_f]$, the HB3 results do not improve on the HB1 results, for example, Fig. 10a, and may indeed be worse, for example, Figs. 10b and 14. For the second branch, the HB3 results match the time integration results well.

V. Conclusions

The LCOs of a two-dimensional airfoil, including a control surface with freeplay restoring force, are investigated. A simple theoretical model is used, and the results are close to those of the previous theoretical models and the experimental data. Furthermore, in the time integration results, some new phenomena are discovered, namely, the hysteresis of the first bifurcation and the unusual effect of the initial conditions. The earlier DF and linearization (HB1) approaches are reformulated in such a way that more harmonics are easily included. A general derivation of the HB technique including a finite number of harmonics is developed specifically for the freeplay model. The first and third harmonic approximations, HB1 and HB3, are applied to the aeroelastic three degrees-of freedom system with the set of system parameters given in a previous experiment. In the HB1 approach, a single polynomial equation for the fundamental frequency is obtained, and the solutions of the Fourier coefficients are explicitly expressed in terms of the frequency. The HB1 results are essentially identical to the previous DF results, whereas the computational cost is reduced. In the HB3 approach, a system of the frequency and two augmented variables are obtained, and the solutions of the Fourier coefficients are explicit functions of the frequency and the two augmented variables. Generally, the HB3 results improve on the HB1 results and are in an excellent agreement with the time integration results. In general, by the use of the higher-order HB method, the system of unknowns, that is, the Fourier components, the fundamental frequency, and the two augmented variables, can always be reduced to a system of three equations in the frequency and the two augmented variables. The Fourier coefficients can then be calculated directly from the explicit expressions for these three variables determined from the reduced system.

Appendix A: Definitions of System Parameters

The following system parameter definitions have been adapted from Ref. 10:

The ratio of the mass of a cylinder of air having a diameter equal to the chord of the wing to the mass of the wing, both per unit span is $\kappa = \pi\rho b^2/M$.

The radius of gyration divided by b is $r_\alpha = \sqrt{I_\alpha/Mb^2}$.

The center of gravity distance of the wing from a, divided by b is $x_\alpha = S_\alpha/Mb$.

The uncoupled natural frequency of torsional vibration around a is $\bar{\omega}_\alpha = \sqrt{C_\alpha/I_\alpha}$.

The reduced radius of gyration of the aileron divided by b, that is, the radius at which the entire mass of the airfoil would have to be concentrated to give the moment of inertia of the aileron I_β is $r_\beta = \sqrt{I_\beta/Mb^2}$.

The reduced center of gravity distance from c is $x_\beta = S_\beta/Mb$.

The uncoupled natural frequency of torsional vibration of the aileron around c is $\bar{\omega}_\beta = \sqrt{C_\beta/I_\beta}$.

The uncoupled natural frequency of the wing in deflection is $\bar{\omega}_h = \sqrt{C_h/M}$.

Appendix B: Theodorsen Constants

$$T_1 = -\tfrac{1}{3}\sqrt{1-c^2}(2+c^2) + c\cos^{-1}c$$

$$T_2 = c(1-c^2) - \sqrt{1-c^2}(1+c^2)\cos^{-1}c + c(\cos^{-1}c)^2$$

$$T_3 = -\left(\tfrac{1}{8}+c^2\right)(\cos^{-1}c)^2 + \tfrac{1}{4}c\sqrt{1-c^2}(\cos^{-1}c)(7+2c^2) - \tfrac{1}{8}(1-c^2)(5c^2+4)$$

$$T_4 = -\cos^{-1}c + c\sqrt{1-c^2}$$

$$T_5 = -(1-c^2) - (\cos^{-1}c)^2 + 2c\sqrt{1-c^2}\cos^{-1}c$$

$$T_6 = T_2$$

$$T_7 = -\left(\tfrac{1}{8}+c^2\right)\cos^{-1}c + \tfrac{1}{8}c\sqrt{1-c^2}(7+2c^2)$$

$$T_8 = -\tfrac{1}{3}\sqrt{1-c^2}(2c^2+1) + c\cos^{-1}c$$

$$T_9 = \tfrac{1}{2}\left[\tfrac{1}{3}\left(\sqrt{1-c^2}\right)^3 + aT_4\right] = \tfrac{1}{2}(-p + aT_4), \qquad p = -\tfrac{1}{3}\left(\sqrt{1-c^2}\right)^3$$

$$T_{10} = \sqrt{1-c^2} + \cos^{-1}c$$

$$T_{11} = (\cos^{-1}c)(1-2c) + \sqrt{1-c^2}(2-c)$$

$$T_{12} = \sqrt{1-c^2}(2+c) - (\cos^{-1}c)(2c+1)$$

$$T_{13} = \tfrac{1}{2}\left[-T_7 - (c-a)T_1\right]$$

$$T_{14} = \tfrac{1}{16} + \tfrac{1}{2}ac$$

Appendix C: Expressions of the Coefficients of System (6)

$$A_1 = r_\alpha^2 + \kappa\left(\tfrac{1}{8}+a^2\right)$$

$$A_2 = r_\beta^2 + (c-a)x_\beta - (\kappa/\pi)(c-a)T_1 - (\kappa/\pi)T_7$$

$$A_3 = x_\alpha - a\kappa$$

$$A_4 = \kappa\left(\tfrac{1}{2}-a\right) - 2\kappa\left(a+\tfrac{1}{2}\right)\left(\tfrac{1}{2}-a\right)(1-\psi_1-\psi_2) + s_{11}(b/U)$$

$$A_5 = (\kappa/\pi)\left[-2p - \left(\tfrac{1}{2}-a\right)T_4 - \left(a+\tfrac{1}{2}\right)(1-\psi_1-\psi_2)\right] + s_{12}(b/U)$$

$$A_6 = -2\kappa\left(a+\tfrac{1}{2}\right)(1-\psi_1-\psi_2) + s_{13}(b/U)$$

$$A_7 = r_\alpha^2\omega_\alpha^2(1/U)^2 - 2\kappa\left(a+\tfrac{1}{2}\right)\left[1-\psi_1-\psi_2 + \left(\tfrac{1}{2}-a\right)(\psi_1\epsilon_1+\psi_2\epsilon_2)\right]$$

$$A_8 = (\kappa/\pi)(T_4+T_{10}) - 2(\kappa/\pi)\left(a+\tfrac{1}{2}\right)\left[T_{10}(1-\psi_1-\psi_2) + \tfrac{1}{2}T_{11}(\psi_1\epsilon_1+\psi_2\epsilon_2)\right]$$

$$A_9 = -2\kappa\left(a+\tfrac{1}{2}\right)(\psi_1\epsilon_1+\psi_2\epsilon_2)$$

$$A_{11} = -2\kappa\left(a+\tfrac{1}{2}\right)\left[\psi_1\epsilon_1 - \left(\tfrac{1}{2}-a\right)\psi_1\epsilon_1^2\right]$$

$$A_{12} = -2\kappa\left(a+\tfrac{1}{2}\right)\left[\psi_2\epsilon_2 - \left(\tfrac{1}{2}-a\right)\psi_2\epsilon_2^2\right]$$

$$A_{13} = -2(\kappa/\pi)\left(a+\tfrac{1}{2}\right)\left(T_{10}\psi_1\epsilon_1 - \tfrac{1}{2}T_{11}\psi_1\epsilon_1^2\right)$$

$$A_{14} = -2(\kappa/\pi)\left(a+\tfrac{1}{2}\right)\left(T_{10}\psi_2\epsilon_2 - \tfrac{1}{2}T_{11}\psi_2\epsilon_2^2\right)$$

$$A_{15} = 2\kappa\left(a+\tfrac{1}{2}\right)\psi_1\epsilon_1^2, \qquad A_{16} = 2\kappa\left(a+\tfrac{1}{2}\right)\psi_2\epsilon_2^2$$

$$B_1 = r_\beta^2 + (c-a)x_\beta + 2(\kappa/\pi)T_{13}, \qquad B_2 = r_\beta^2 - (\kappa/\pi^2)T_3$$

$$B_3 = x_\beta - (\kappa/\pi)T_1$$

$$B_4 = (\kappa/\pi)\Big[p - T_1 - \tfrac{1}{2}T_4 + T_{12}\Big(\tfrac{1}{2} - a\Big) \times (1 - \psi_1 - \psi_2)\Big] + s_{21}(b/U)$$

$$B_5 = (\kappa/2\pi^2)\Big[- T_4T_{11} + T_{12}T_{11}(1 - \psi_1 - \psi_2)\Big] + s_{22}(b/U)$$

$$B_6 = (\kappa/\pi)T_{12}(1 - \psi_1 - \psi_2) + s_{23}(b/U)$$

$$B_7 = (\kappa/\pi)T_{12}\Big[1 - \psi_1 - \psi_2 + \Big(\tfrac{1}{2} - a\Big)(\psi_1\epsilon_1 + \psi_2\epsilon_2)\Big]$$

$$B_8 = r_\beta^2\omega_\beta^2(1/U)^2 + (\kappa/\pi^2)(T_5 - T_4T_{10}) + (\kappa/\pi^2)T_{12}\Big[T_{10}(1 - \psi_1 - \psi_2) + T_{11}(\psi_1\epsilon_1 + \psi_2\epsilon_2)\Big]$$

$$B_9 = (\kappa/\pi)T_{12}(\psi_1\epsilon_1 + \psi_2\epsilon_2)$$

$$B_{11} = (\kappa/\pi)T_{12}\Big(\psi_1\epsilon_1 - \Big(\tfrac{1}{2} - a\Big)\psi_1\epsilon_1^2\Big)$$

$$B_{12} = (\kappa/\pi)T_{12}\Big(\psi_2\epsilon_2 - \Big(\tfrac{1}{2} - a\Big)\psi_2\epsilon_2^2\Big)$$

$$B_{13} = (\kappa/\pi^2)T_{12}\Big(T_{10}\psi_1\epsilon_1 - T_{11}\psi_1\epsilon_1^2\Big)$$

$$B_{14} = (\kappa/\pi^2)T_{12}\Big(T_{10}\psi_2\epsilon_2 - T_{11}\psi_2\epsilon_2^2\Big)$$

$$B_{15} = -(\kappa/\pi)T_{12}\psi_1\epsilon_1^2, \qquad B_{16} = -(\kappa/\pi)T_{12}\psi_2\epsilon_2^2$$

$$C_1 = x_\alpha - a\kappa, \qquad C_2 = x_\beta - (\kappa/\pi)T_1, \qquad C_3 = M_{\text{total}}/M + \kappa$$

$$C_4 = \kappa\Big[1 + 2\Big(\tfrac{1}{2} - a\Big)(1 - \psi_1 - \psi_2)\Big] + s_{31}(b/U)$$

$$C_5 = (\kappa/\pi)\Big[- T_4 + T_{11}(1 - \psi_1 - \psi_2)\Big] + s_{32}(b/U)$$

$$C_6 = 2\kappa(1 - \psi_1 - \psi_2) + s_{33}(b/U)$$

$$C_7 = 2\kappa\Big[1 - \psi_1 - \psi_2 + \Big(\tfrac{1}{2} - a\Big)(\psi_1\epsilon_1 + \psi_2\epsilon_2)\Big]$$

$$C_8 = 2(\kappa/\pi)\Big[T_{10}(1 - \psi_1 - \psi_2) + \tfrac{1}{2}T_{11}(\psi_1\epsilon_1 + \psi_2\epsilon_2)\Big]$$

$$C_9 = \omega_\xi^2(1/U)^2 + 2\kappa(\psi_1\epsilon_1 + \psi_2\epsilon_2)$$

$$C_{11} = 2\kappa\Big[\psi_1\epsilon_1 - \Big(\tfrac{1}{2} - a\Big)\psi_1\epsilon_1^2\Big]$$

$$C_{12} = 2\kappa\Big[\psi_2\epsilon_2 - \Big(\tfrac{1}{2} - a\Big)\psi_2\epsilon_2^2\Big]$$

$$C_{13} = 2(\kappa/\pi)\Big(T_{10}\psi_1\epsilon_1 - \tfrac{1}{2}T_{11}\psi_1\epsilon_1^2\Big)$$

$$C_{14} = 2(\kappa/\pi)\Big(T_{10}\psi_2\epsilon_2 - \tfrac{1}{2}T_{11}\psi_2\epsilon_2^2\Big)$$

$$C_{15} = -2\kappa\psi_1\epsilon_1^2, \qquad C_{16} = -2\kappa\psi_2\epsilon_2^2$$

Appendix D: Fourier Components for the Flap and the Plunge Motions

The Fourier components of the time derivatives and the integral terms for the flap rotation and the plunge deflection motions are

$$\beta' = -\omega c_1 \sin\omega\tau + n\omega\sum_{n=2}^{N}(c_n\cos n\omega\tau - d_n\sin n\omega\tau)$$

$$\xi' = n\omega\sum_{n=1}^{N}(e_n\cos n\omega\tau - f_n\sin n\omega\tau)$$

$$\beta'' = -\omega^2 c_1\cos\omega\tau - n^2\omega^2\sum_{n=2}^{N}(c_n\sin n\omega\tau + d_n\cos n\omega\tau)$$

$$\xi'' = -n^2\omega^2\sum_{n=1}^{N}(e_n\sin n\omega\tau + f_n\cos n\omega\tau)$$

$$w_3 = \frac{c_0}{\varepsilon_1} + \frac{c_1}{\varepsilon_1^2 + \omega^2}(\varepsilon_1\cos\omega\tau + \omega\sin\omega\tau) + \sum_{n=2}^{N}\frac{\varepsilon_1}{\varepsilon_1^2 + (n\omega)^2}(c_n\sin n\omega\tau + d_n\cos n\omega\tau) + \sum_{n=1}^{N}\frac{n\omega}{\varepsilon_1^2 + (n\omega)^2}(d_n\sin n\omega\tau - c_n\cos n\omega\tau)$$

$$w_4 = \frac{c_0}{\varepsilon_2} + \frac{c_1}{\varepsilon_2^2 + \omega^2}(\varepsilon_2\cos\omega\tau + \omega\sin\omega\tau) + \sum_{n=2}^{N}\frac{\varepsilon_2}{\varepsilon_2^2 + (n\omega)^2}(c_n\sin n\omega\tau + d_n\cos n\omega\tau) + \sum_{n=1}^{N}\frac{n\omega}{\varepsilon_2^2 + (n\omega)^2}(d_n\sin n\omega\tau - c_n\cos n\omega\tau)$$

$$w_5 = \frac{e_0}{\varepsilon_1} + \sum_{n=1}^{N}\frac{\varepsilon_1}{\varepsilon_1^2 + (n\omega)^2}(e_n\sin n\omega\tau + f_n\cos n\omega\tau) + \sum_{n=1}^{N}\frac{n\omega}{\varepsilon_1^2 + (n\omega)^2}(f_n\sin n\omega\tau - e_n\cos n\omega\tau)$$

$$w_6 = \frac{e_0}{\varepsilon_2} + \sum_{n=1}^{N}\frac{\varepsilon_2}{\varepsilon_2^2 + (n\omega)^2}(e_n\sin n\omega\tau + f_n\cos n\omega\tau) + \sum_{n=1}^{N}\frac{n\omega}{\varepsilon_2^2 + (n\omega)^2}(f_n\sin n\omega\tau - e_n\cos n\omega\tau)$$

Appendix E: Fourier Coefficients of the Response Force for Cases in Section IV.B

For $N = 1$, the first three Fourier coefficients are

$$M_0 = [-t_1\cos t_1 + (t_2 - \pi)\cos t_2 + \sin t_1 - \sin t_2](c_1/\pi)$$

$$M_{s_1} = 0$$

$$M_{c_1} = (-\cos t_1\sin t_1 + \cos t_2\sin t_2 + t_1 + \pi - t_2)(c_1/\pi) \quad \text{(E1)}$$

For $N = 3$, the first five Fourier coefficients are

$$M_0 = [-t_1\cos t_1 + (t_2 - \pi)\cos t_2 + \sin t_1 - \sin t_2](c_1/\pi) + [(t_2 - \pi)\sin(3t_2) - t_1\sin(3t_1)](c_3/\pi) + \Big[- t_1\cos(3t_1) + (t_2 - \pi)\cos(3t_2) - \tfrac{1}{3}\sin t_1 - \tfrac{4}{3}\sin t_2\cos^2 t_2 + \tfrac{4}{3}\sin t_1\cos^2 t_1 + \tfrac{1}{3}\sin t_2\Big](d_3/\pi)$$

$$M_{s_1} = \Big(2\sin t_1\cos t_1 - 2\sin t_1\cos^3 t_1 - 2\sin t_2\cos t_2 + 2\sin t_2\cos^3 t_2\Big)(c_3/\pi)$$

$$M_{c_1} = \Big(- \cos t_1\sin t_1 + \cos t_2\sin t_2 + t_1 + \pi - t_2\Big)(c_1/\pi) + \Big[2\sin t_2\sin(3t_2) - 2\sin t_1\sin(3t_1)\Big](c_3/\pi) + \Big[- 2\sin t_1\cos(3t_1) - 2\sin t_2\cos^3 t_2 + 2\sin t_2\cos(3t_2) + 2\sin t_1\cos^3 t_1\Big](d_3/\pi)$$

$$
\begin{aligned}
M_{s_3} &= \left(\tfrac{16}{3}\sin t_2\cos^5 t_2 - \tfrac{16}{3}\sin t_2\cos^3 t_2 + \sin t_2\cos t_2 - t_2\right.\\
&\quad - \tfrac{16}{3}\sin t_1\cos^5 t_1 + \tfrac{16}{3}\sin t_1\cos^3 t_1\\
&\quad \left. - \sin t_1\cos t_1 + t_1 + \pi\right)(c_3/\pi)\\
M_{c_3} &= \left[\left(-\tfrac{8}{3}\sin t_1\cos^2 t_1 + \tfrac{2}{3}\sin t_1\right)\cos t_1 + 2\sin t_1\cos^3 t_1\right.\\
&\quad - 2\sin t_2\cos^3 t_2 + \left(\tfrac{8}{3}\sin t_2\cos^2 t_2 - \tfrac{2}{3}\sin t_2\right)\cos t_2\Big](c_1/\pi)\\
&\quad + \left[\left(\tfrac{8}{3}\sin t_2\cos^2 t_2 - \tfrac{2}{3}\sin t_2\right)\sin(3t_2) + \left(-\tfrac{8}{3}\sin t_1\cos^2 t_1\right.\right.\\
&\quad \left.\left. + \tfrac{2}{3}\sin t_1\right)\sin(3t_1)\Big](c_3/\pi) + \Big[\left(\tfrac{8}{3}\sin t_2\cos^2 t_2 - \tfrac{2}{3}\sin t_2\right)\right.\\
&\quad \left. \times \cos(3t_2) + \tfrac{16}{3}\sin t_2\cos^3 t_2 - t_2 + \pi - \tfrac{16}{3}\sin t_2\cos^5 t_2\right.\\
&\quad - \tfrac{16}{3}\sin t_1\cos^3 t_1 + \sin t_1\cos t_1 + t_1 + \tfrac{16}{3}\sin t_1\cos^5 t_1\\
&\quad \left. - \sin t_2\cos t_2 + \left(-\tfrac{8}{3}\sin t_1\cos^2 t_1 + \tfrac{2}{3}\sin t_1\right)\cos(3t_1)\right](d_3/\pi)
\end{aligned}
\tag{E2}
$$

References

[1]Woolston, D. S., Runyan, H. L., and Andrews, R. E., "An Investigation of Fffects of Certain Types of Structural Nonlinearities on Wing and Control Surface Flutter," *Journal of Aeronautical Science*, Vol. 24, No. 1, 1957, pp. 57–63.

[2]Shen, S. F., "An Approximate Analysis of Nonlinear Flutter Problems," *Journal of the Aerospace Sciences*, Vol. 26, No. 1, 1959, pp. 25–32.

[3]Küssner, H. G., "On the Nonlinear Approach to the Aeroelastic Stability Theory," AGARD Rept. 246, April 1959.

[4]Lee, B. H. K., Price, S. J., and Wong, Y. S., "Nonlinear Aeroelastic Analysis of Airfoils: Bifurcation and Chaos," *Progress in Aerospace Science*, Vol. 35, No. 3, 1999, pp. 205–334.

[5]Tang, D., Dowell, E. H., and Virgin, L. N., "Limit Cycle Behaviour of an Airfoil with a Control Surface," *Journal of Fluids and Structure*, Vol. 12, No. 7, 1998, pp. 839–858.

[6]Laurenson, R. M., and Trn, R. M., "Flutter Analysis of Missile Control Surfaces Containing Structural Nonlinearities," *AIAA Journal*, Vol. 18, No. 10, 1980, pp. 1245–1251.

[7]Liu, L., and Dowell, E. H., "The Secondary Bifurcation of an Aeroelastic Airfoil Motion with Cubic Restoring Forces," *Nonlinear Dynamics*, Vol. 37, No. 1, 2004, pp. 31–49.

[8]Conner, M. D., Tang, D. M., Dowell, E. H., and Virgin, L. N., "Nonlinear Behaviour of a Typical Airfoil Section with Control Surface Freeplay: a Numerical and Experimental Study," *Journal of Fluids and Structure*, Vol. 11, 1997, pp. 89–109.

[9]Tang, D. M., Conner, M. D., and Dowell, E. H., "Reduced-Order Finite State Airload and Its Applications to a Nonlinear Aeroelastic System," *Journal of Aircraft*, Vol. 35, 1998, pp. 332–338.

[10]Theodorsen, T., "General Theory of Aerodynamic Instability and the Mechanism of Flutter," NACA Rept. 496, 1935.

[11]Jones, R. T., "The Unsteady Lift of a Wing of Finite Aspect Ratio," NACA Rept. 681, 1940.

[12]Hénon, M., "On the Numerical Computation of Poincaré Maps," *Physica D*, Vol. 5, No. 2–3, 1982, pp. 412–414.

[13]Conner, M. D., Donescu, P., and Virgin, L. N., "On the Global Convergence Characteristics of Numerically Evaluated Jabobian Matrices," *Nonlinear Dynamics*, Vol. 10, No. 2–3, 1996, pp. 165–174.

[14]Conner, M. D., Virgin, L. N., and Dowell, E. H., "Accurate Numerical Integration of State-Space Models for Aeroelastic Systems with Freeplay," *AIAA Journal*, Vol. 34, No. 11, 1996, pp. 2202–2205.

[15]Bayly, P. V., and Virgin, L. N., "Chaotic Rattling of a Piecewise Nonlinear Oscillator," ASME 91-WA-DEC-17, 1991.

[16]Lin, W. B., and Cheng, W. H., "Nonlinear Flutter of Loaded Lifting Surfaces (I) and (II)," *Journal of the Chinese Society of Mechanical Engineers*, Vol. 14, No. 5, 1993, pp. 446–466.

[17]Liu, L., Wong, Y. S., and Lee, B. H. K., "Nonlinear Aeroelastic Analysis Using the Point Transformation Method, Part 1 and Part 2," *Journal of Sound and Vibration*, Vol. 253, No.2, 2002, pp. 447–483.

[18]Monagan, M. B., Geddes, K. O., Heal, K. M., Lebahn, G., Vorkoetter, J., and McCarron, J., *Maple 6 Programming Guide*, Waterloo Maple, Inc., Waterloo, ON, Canada, 2000.

C. Pierre
Associate Editor